AIAA JOURNAL
Vol. 43, No. 1, January 2005

Temporal Linear Stability Analysis of Three-Dimensional Compressible Binary Shear Layers

Ivan Fedioun* and Nicolas Lardjane†
Centre National de la Recherche Scientifique, 45071 Orleans Cedex 2, France

Temporal linear stability analysis is performed on the three-dimensional compressible binary shear layer for density ratios ranging from 1 to 32 and convective Mach numbers up to 2. Comparison is made with the results of spatial theory. Some stability properties are shared by both approaches, for example, the independence of the direction of propagation of the most unstable modes from the freestream density ratio, but other features are different: a single secondary mode appears instead of two at high compressibility. An empirical model is proposed for the wave length and phase speed of the most amplified waves. Direct numerical simulations show good agreement with linear inviscid theory for initial Reynolds numbers greater than 400.

I. Introduction

In many applications, efficient mixing of two different gases is a crucial issue, which mainly depends on instability properties of shear flows. For such flows, the main way to achieve rapid homogeneization is to trigger the transition to turbulence. Nevertheless, this is a nontrivial task in supersonic flows, especially when the gases have very different densities, such as air/H_2 in scramjet combustion chambers. Gutmark et al.[1] have listed both active and passive devices for the excitation of supersonic free-shear flows. The frequencies (spatial or temporal) involved are always linked to the most amplified modes of the flow, which can be predicted by linear stability theory. The enhanced stability of compressible mixing layers with increasing Mach number and density ratio is a real problem for the direct numerical simulation of such flows too, because classical perturbation techniques (superposition of low-amplitude white noise) are inefficient for a rapid laminar/turbulent transition, leading to a waste of CPU time.

Linear stability analysis is a well-established technique since the pioneering works of Rayleigh, Orr, and Sommerfeld, and many classical textbooks are devoted to the subject (e.g., Ref. 2). Concerning free-shear flows, both temporal and spatial stability of the hyperbolic tangent profile has been studied in the incompressible case by Michalke,[3,4] whose results have been extensively used in numerical simulations (e.g., Refs. 5 and 6). In the mid-1970s, Blumen et al.[7] investigated the temporal stability of the compressible hyperbolic tangent shear layer up to $M_c = 2$ and discovered a second unstable mode above $M_c = 1$. More recently, using an asymptotic theory, Balsa and Goldstein[8] extended the work of Blumen et al. to infinite M_c. The same year, Sandham and Reynolds[9] compared the spatial amplification predicted by the linear stability theory to the experimental growth rate measured by Brown and Roshko,[10] reproducing the density ratios by heating a mono-species shear layer. They found a global linear fit between the experimental growth rate and the predicted amplification factor. Jackson and Grosch have extensively studied the effects of temperature distribution and convective Mach number on the spatial stability of single-gas mixing layers, for both two-dimensional[11,12] and three-dimensional[13] systems, before turning to binary mixing systems.[14] In this last paper, they defined a new kind of convective Mach number, which corresponds to the classical definition of Papamoschou and Rosko (see, e.g., Ref. 15) if the heat-capacity ratio is the same for both gases. They also provided the chart in the velocity–temperature ratio plane for absolute or convective instability at variable Mach numbers. Although the effect of three-dimensional disturbances was mentioned, their study was essentially two-dimensional, the mean flow being approximated by a hyperbolic tangent profile. A few years latter, Kozusko et al.[16,17] extended the work of Jackson and Grosch to a wider set of binary systems and showed that the structure of the mean flow has a crucial effect on its stability properties. The mean flow was obtained from a Levy–Lees self-similar solution. Nevertheless, this study was still two-dimensional. The effect of heat release on the stability, both spatial and temporal, of the reacting mixing layer was studied by Shin and Ferziger[18] in the low-Mach number two-dimensional case. In the spatial case, two unstable "outer" modes can emerge at large enough heat release and may overcome the central mode, which is damped by the heating effect. However, no explicit reference to the freestream density ratio was made in this paper. The most complete parametric study of compressibility, heat release, density, and velocity ratio effects is that of Day et al.[19] in the spatial case. They provided the regime charts for unstable modes in a wide range of these parameters and used the eigenfunction energy profiles to describe the mechanisms that destabilize the mixing layer in each case.

The aim of this paper is to complete the work of these previous authors by the temporal stability analysis of three-dimensional binary mixing layers with variable thermodynamic and transport properties. This is useful for setting clever initial conditions in temporal direct numerical simulations of high-density-ratio compressible mixing layers. Because many combinations of gases have already been investigated, we will focus only on two extreme pairs, O_2/N_2, and O_2/H_2, which are enough to illustrate three-dimensional effects. Moreover, we will not consider sweep effects due to the relative directions of free streams (denoted by angle ϕ in Ref. 13). In Sec. II, the temporal approach will be discussed in reference to absolute/convective instability, and the mean-flow profile will be described. The temporal stability equations and the method of solution will be derived in Sec. III. Section IV will show the effects of the convective Mach number and density ratio on the emergence of oblique and double-valued unstable modes. A model for the wavelength and phase speed of the most amplified modes is then proposed. Section V will compare the predicted amplification factors to direct numerical simulation (DNS) results, in both two and three dimensions, and will show the limits of the inviscid linear theory.

II. Mean Flow

Consider the plane coflowing mixing layer generated by two gases issuing at different velocities from a splitter plate (Fig. 1). Referring

Received 22 July 2003; revision received 12 July 2004; accepted for publication 20 July 2004.

*Associate Professor, Laboratoire de Combustion et Systèmes Réactifs, 1C, avenue de la Recherche Scientifique; fedioun@cnrs-orleans.fr.

†Research Scientist, Laboratoire de Combustion et Systèmes Réactifs; currently Research Scientist, Commissariat à l'Energie Atomique/Direction des Applications Militaires, B.P. 12, 91680 Bruyères-la-Châtel, France.

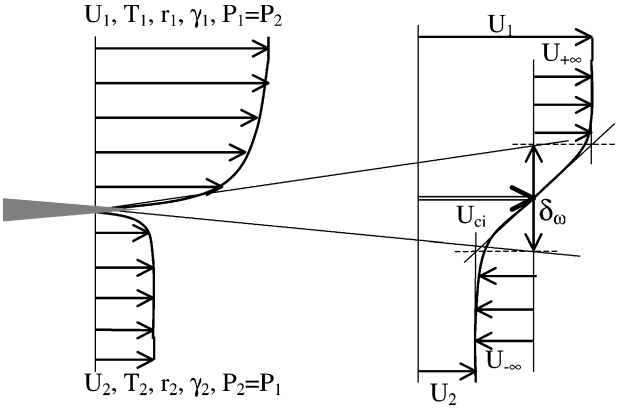

Fig. 1 Coflowing mixing layer.

to the upper flow with subscript 1 and to the lower one with subscript 2 and assuming that $\gamma_1 = \gamma_2$, the convective velocity

$$U_c = \frac{a_2 U_1 + a_1 U_2}{a_1 + a_2} \tag{1}$$

(with a the speed of sound) is the velocity at which the coherent structures are convected away from the plate. The most suitable compressibility-effect parameter is the convective Mach number,[15,20] defined as

$$M_c = \frac{U_1 - U_c}{a_1} = \frac{U_c - U_2}{a_2} = \frac{\Delta U}{a_1 + a_2} \tag{2}$$

where $\Delta U = U_1 - U_2$. A major breakthrough in the stability properties of such flow has been made by Huerre and Monkewitz,[21] who applied the Briggs–Bers criterion to define the conditions for absolute or convective instability. It was shown that unless a large enough counterflow is present,

$$R = \frac{U_1 - U_2}{U_1 + U_2} > 1.315, \qquad U_2 < 0 \tag{3}$$

the constant-density mixing layer is convectively unstable and, hence, the spatial theory applies. Absolute instability occurs only in case of large counterflow, and temporally evolving disturbances have then to be considered. Pavithran and Redekopp[22] and also Jackson and Grosch[14] have computed the absolute/convective transition for the compressible and variable-density (heated) hyperbolic tangent profile: as the density ratio ρ_1/ρ_2 or the Mach number M_1 is increased, more reverse flow is needed for absolute instability. Experimental evidence (Ref. 23, Fig. 18) has confirmed the predicted convective/absolute transition for density ratios up to 6 (incompressible flow). The coflowing reacting mixing layer was found to be convectively unstable whatever the amount of heat release by Shin and Ferziger.[18]

In a moving frame convected at velocity U_c, the upper and lower apparent freestream velocities are $U_1 - U_c$ and $U_c - U_2$. To recover some symmetry, as in the incompressible monospecies case, the incompressible convective velocity $U_{ci} = (U_1 + U_2)/2$ is rather used for the moving reference frame,[10] so that the apparent freestream velocities are $U_{+\infty} = U_1 - U_{ci} = \Delta U/2 = -U_{-\infty}$. Owing to diffusion of one flow into the other, the vorticity thickness

$$\delta_\omega = \Delta U \Big/ \left(\frac{\partial u}{\partial y}\right)_{\max} \tag{4}$$

of the mixing layer increases with downstream distance from the splitter plate in the laboratory frame, or with time in the moving reference frame. Numerical simulations of transitional mixing layers in the moving reference frame, that is, temporal simulations (with periodic boundary conditions in the flow direction), show poor agreement with experimental growth rates.[5,9] It should rather compare with countercurrent mixing layers, having infinite counterflow $R \to \infty$ and absolute rather than convective instability. In this case, to which this paper is devoted, temporal stability theory should be used.

The equations of motion for the flow are Navier–Stokes equations. Cast in nonconservation form, using Einstein's summation convention, they read, for a mixture,

$$\frac{\partial \rho}{\partial t} + \rho u_{j,j} + \rho_{,j} u_j = 0 \tag{5}$$

$$\rho\left(\frac{\partial u_i}{\partial t} + u_{i,j} u_j\right) = -p_{,i} + \tau_{ij,j} \tag{6}$$

$$\rho\left(\frac{\partial e}{\partial t} + e_{,j} u_j\right) = -pu_{j,j} - q_{j,j} + u_{i,j}\tau_{ij} \tag{7}$$

$$\rho\left(\frac{\partial Y_\alpha}{\partial t} + Y_{\alpha,j} u_j\right) = -J_{\alpha j,j} \tag{8}$$

If the mixture is newtonian and obeys the Stokes hypothesis, the viscous stress is

$$\tau_{ij} = \mu\left(u_{i,j} + u_{j,i} - \tfrac{2}{3} u_{k,k}\delta_{ij}\right) \tag{9}$$

Neglecting the Dufour effect, the heat flux results from partial enthalpy fluxes and from the Fourier law,

$$q_j = \sum_\alpha h_\alpha J_{\alpha j} - \kappa T_{,j} \tag{10}$$

and the mass flux of species α (neglecting the Soret effect) follows Fick's law,

$$J_{\alpha j} = -\rho D_{\alpha m} Y_{\alpha,j} \tag{11}$$

Assuming perfect gases, the equation of state of the mixture is

$$p = \rho \mathcal{R} T \sum_\alpha \frac{Y_\alpha}{W_\alpha} = \rho r T \tag{12}$$

where $\mathcal{R}$ is the universal gas constant, r the mixture constant, and W_α the molecular weight of the species α. Partial enthalpies are given by

$$h_\alpha = \Delta h_\alpha^0 + \int_{T_0}^{T} C p_\alpha(\theta)\, \mathrm{d}\theta \tag{13}$$

and the internal energy of the mixture follows $\mathrm{d}e = C_v\, \mathrm{d}T$ with $C_v = \sum_\alpha Y_\alpha C v_\alpha(T)$.

The linear stability analysis is performed for the mean flow obtained from a self-similar solution of the temporal (rather than spatial) boundary-layer approximation of Eqs. (5–8), limited to a binary mixture, with variable transport coefficients and thermodynamic properties. It depends only on the freestream velocity difference ΔU and thermodynamic properties, and it reduces, in the incompressible monospecies limit, to

$$u = \Delta U / 2\mathrm{erf}\left[\sqrt{\pi}(y/\delta_\omega)\right] \tag{14}$$

The influence of molecular weight, heating, and compressibility on the flow characteristics is detailed in Ref. 24. For the stability problem, the flow is assumed parallel, homogeneous in the spanwise z direction, at constant pressure. It is given the subscript s (for similarity); thus

$$v_s(y, t) = w_s(y, t) = 0 \tag{15}$$

$$p_s(y, t) = P = \text{cste} \tag{16}$$

III. Linear Inviscid Temporal Stability Analysis

A. Perturbation Equations

Because viscous fluxes [Eqs. (9–11)] are highly nonlinear in the compressible binary case, the stability analysis is performed under the inviscid approximation of Eqs. (5–8) for a binary $\text{gas}_1/\text{gas}_2$ mixture:

$$\frac{\partial \rho}{\partial t}+\frac{\partial \rho u}{\partial x}+\frac{\partial \rho v}{\partial y}+\frac{\partial \rho w}{\partial z}=0 \tag{17}$$

$$\rho\left(\frac{\partial u}{\partial t}+u\frac{\partial u}{\partial x}+v\frac{\partial u}{\partial y}+w\frac{\partial u}{\partial z}\right)+\frac{\partial p}{\partial x}=0 \tag{18}$$

$$\rho\left(\frac{\partial v}{\partial t}+u\frac{\partial v}{\partial x}+v\frac{\partial v}{\partial y}+w\frac{\partial v}{\partial z}\right)+\frac{\partial p}{\partial y}=0 \tag{19}$$

$$\rho\left(\frac{\partial w}{\partial t}+u\frac{\partial w}{\partial x}+v\frac{\partial w}{\partial y}+w\frac{\partial w}{\partial z}\right)+\frac{\partial p}{\partial z}=0 \tag{20}$$

$$\rho C_v\left(\frac{\partial T}{\partial t}+u\frac{\partial T}{\partial x}+v\frac{\partial T}{\partial y}+w\frac{\partial T}{\partial z}\right)+p\left(\frac{\partial u}{\partial x}+\frac{\partial v}{\partial y}+\frac{\partial w}{\partial z}\right)=0 \tag{21}$$

$$\rho\left(\frac{\partial Y}{\partial t}+u\frac{\partial Y}{\partial x}+v\frac{\partial Y}{\partial y}+w\frac{\partial Y}{\partial z}\right)=0 \tag{22}$$

In Eq. (22), $Y=Y_1=1-Y_2$. Thus, the gas constant is

$$r=r_2+(r_1-r_2)Y=(\gamma-1)C_v \tag{23}$$

with

$$C_v=C_{v_2}+(C_{v_1}-C_{v_2})Y \tag{24}$$

The mean flow is now perturbed with a low-amplitude field denoted by the suffix "$_0$," so that the instantaneous three-dimensional flowfield is

$$\begin{aligned}
\rho(x,y,z,t) &= \rho_0(x,y,z,t)+\rho_s(y,t)\\
u(x,y,z,t) &= u_0(x,y,z,t)+u_s(y,t)\\
v(x,y,z,t) &= v_0(x,y,z,t)\\
w(x,y,z,t) &= w_0(x,y,z,t)\\
p(x,y,z,t) &= p_0(x,y,z,t)+P\\
T(x,y,z,t) &= T_0(x,y,z,t)+T_s(y,t)\\
Y(x,y,z,t) &= Y_0(x,y,z,t)+Y_s(y,t)
\end{aligned} \tag{25}$$

Perturbations are assumed to be sine waves of wave number $2\pi/\alpha$, propagating at velocity c in the (x,z) plane at angle θ relative to the x axis (Fig. 2), whose (complex) amplitude depends only on y. For instance,

$$\rho_0(x,y,z,t)=\widehat{\rho_0}(y)\exp\{j\alpha(x\cos\theta+z\sin\theta-ct)\} \tag{26}$$

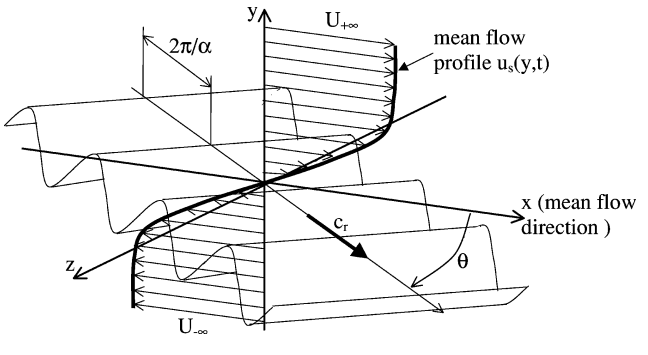

Fig. 2 Sketch of mean flow and three-dimensional perturbation.

Injecting Eqs. (25) into Eqs. (17–22) leads, after linearization, to the eigenvalue ordinary differential system of equations for the perturbation amplitudes:

$$j\alpha(u_s\cos\theta-c)\widehat{\rho_0}+\rho_s'\widehat{v_0}+\rho_s(j\alpha(\widehat{u_0}\cos\theta+\widehat{w_0}\sin\theta)+\widehat{v_0}')=0 \tag{27}$$

$$j\alpha\rho_s(u_s\cos\theta-c)\widehat{u_0}+\rho_s u_s'\widehat{v_0}+j\alpha\widehat{p_0}\cos\theta=0 \tag{28}$$

$$j\alpha\rho_s(u_s\cos\theta-c)\widehat{v_0}+\widehat{p_0}'=0 \tag{29}$$

$$j\alpha\rho_s(u_s\cos\theta-c)\widehat{w_0}+j\alpha\widehat{p_0}\sin\theta=0 \tag{30}$$

$$j\alpha(u_s\cos\theta-c)\widehat{T_0}+T_s'\widehat{v_0}+(\gamma-1)T_s(j\alpha(\widehat{u_0}\cos\theta+\widehat{w_0}\sin\theta)+\widehat{v_0}')=0 \tag{31}$$

$$j\alpha(u_s\cos\theta-c)\widehat{Y_0}+\widehat{v_0}Y_s'=0 \tag{32}$$

and the pressure-perturbation amplitude is obtained from the linearized equation of state:

$$\widehat{p_0}=(r_2+(r_1-r_2)Y_s)(\rho_s\widehat{T_0}+\widehat{\rho_0}T_s)+\rho_s T_s(r_1-r_2)\widehat{Y_0} \tag{33}$$

Here, the prime symbol $'$ denotes derivatives with respect to the y physical transverse coordinate. For temporal stability, α is real and $c=c_r+jc_i$. After some algebra, the equation for $\widehat{p_0}$ can be derived, which is well suited to the formulation of boundary conditions:

$$\widehat{p_0}''-\left[\frac{\rho_s'}{\rho_s}+\frac{2u_s'\cos\theta}{(u_s\cos\theta-c)}\right]\widehat{p_0}'-\alpha^2\left[1-\frac{(u_s\cos\theta-c)^2}{a^2}\right]\widehat{p_0}=0 \tag{34}$$

where $a^2=\gamma r T_s$ denotes the local speed of sound in the mixing layer under mean flow conditions.

One could consider only Eq. (34) and solve a second-order boundary-value problem. In fact, it is numerically more convenient to combine Eqs. (27–32) and (34) to derive an initial-value problem (a Cauchy problem) for $\widehat{p_0}$ and $\widehat{v_0}$:

$$(u_s\cos\theta-c)\widehat{v_0}'=u_s'\cos\theta\widehat{v_0}+j\alpha\left(1-(u_s\cos\theta-c)^2/a^2\right)(\widehat{p_0}/\rho_s) \tag{35}$$

$$\widehat{p_0}'=-j\alpha\rho_s(u_s\cos\theta-c)\widehat{v_0} \tag{36}$$

whose solution provides the other unknowns directly.

B. Boundary Conditions and Solution Procedure

In this temporal problem, there is no singularity in Eqs. (35) and (36) at the critical layer, except for neutral modes such that $c_i\approx 0$. At $y\to\pm\infty$, all the gradients of the mean flow vanish, so that Eq. (34) for the pressure amplitude takes the asymptotic form

$$\widehat{p_0}''-\alpha^2 Z\widehat{p_0}=0 \tag{37}$$

where

$$Z=1-\frac{(U_{\pm\infty}\cos\theta-c)^2}{a_{\pm\infty}^2} \tag{38}$$

drives the whole solution from the freestream conditions. The general solution of Eq. (37) is

$$\widehat{p_0}=A_1\exp\left\{\alpha Z^{\frac{1}{2}}y\right\}+A_2\exp\left\{-\alpha Z^{\frac{1}{2}}y\right\} \tag{39}$$

and Eq. (36) also gives

$$\widehat{v_0}=\frac{jA_1Z^{\frac{1}{2}}}{\rho_{s\pm\infty}(U_{\pm\infty}\cos\theta-c)}\exp\left\{\alpha Z^{\frac{1}{2}}y\right\}-\frac{jA_2Z^{\frac{1}{2}}}{\rho_{s\pm\infty}(U_{\pm\infty}\cos\theta-c)}\exp\left\{-\alpha Z^{\frac{1}{2}}y\right\} \tag{40}$$

Separated into real and imaginary part, Z reads

$$\Re Z + j\,\mathrm{Im}Z = 1 - \frac{(U_{\pm\infty}\cos\theta - c_r)^2 - c_i^2}{a^2} + j\frac{2c_i(U_{\pm\infty}\cos\theta - c_r)}{a^2}$$

Because unstable modes are searched for, $c_i \geq 0$. Let us assume that $|c_r| \leq |U_{\pm\infty}|\cos\theta$, which is true in the incompressible monospecies case and which will be checked a posteriori. At the upper freestream $U_{+\infty}\cos\theta > 0$. Hence, whatever the sign of c_r, $\mathrm{Im}Z \geq 0$, so that $\arg Z \in [0, \pi]$ and $\arg Z^{1/2} \in [0, \pi/2]$. It follows that $\Re Z^{1/2} \geq 0$ and the constant A_1 must vanish at $y = +\infty$. At the lower freestream $U_{-\infty}\cos\theta < 0$. Whatever the sign of c_r, this time $\mathrm{Im}Z \leq 0$, so that $\arg Z \in [-\pi, 0]$ and $\arg Z^{1/2} \in [-\pi/2, 0]$. $\Re Z^{1/2}$ is still positive, and it is the constant A_2 that must vanish at $y = -\infty$.

This gives the initial conditions for the Cauchy problem (35) and (36), which read, setting $A_1 = 1$, $A_2 = 0$:

$$\widehat{p}_{0-\infty} = \exp\left\{\alpha Z^{\frac{1}{2}} y_{-\infty}\right\} \tag{41}$$

$$\widehat{v}_{0-\infty} = \frac{jZ^{\frac{1}{2}}}{\rho_{s-\infty}(U_{-\infty}\cos\theta - c)}\exp\left\{\alpha Z^{\frac{1}{2}} y_{-\infty}\right\} \tag{42}$$

Given the mean flow, the stability problem is to find the set $(\alpha, \theta, c_r, c_i)$ such that the numerical integration of Eqs. (35) and (36) from conditions (41) and (42) matches the upper freestream condition $A_1 = 0$ at $y_{+\infty}$. The system (39) and (40) can be solved analytically for (A_1, A_2). It gives at $y_{+\infty}$

$$A_{1+\infty} = \tfrac{1}{2}\left[\widehat{p}_{0+\infty} - j\rho_{s+\infty}Z_{+\infty}^{-\frac{1}{2}}(U_{+\infty}\cos\theta - c)\widehat{v}_{0+\infty}\right] \times \exp\left\{-\alpha Z_{+\infty}^{\frac{1}{2}} y_{+\infty}\right\}$$

$$A_{2+\infty} = \tfrac{1}{2}\left[\widehat{p}_{0+\infty} + j\rho_{s+\infty}Z_{+\infty}^{-\frac{1}{2}}(U_{+\infty}\cos\theta - c)\widehat{v}_{0+\infty}\right] \times \exp\left\{+\alpha Z_{+\infty}^{\frac{1}{2}} y_{+\infty}\right\}$$

Making A_1 vanish at $y_{+\infty}$ is then equivalent to setting

$$\widehat{p}_{0+\infty} - j\rho_{s+\infty}Z_{+\infty}^{-\frac{1}{2}}(U_{+\infty}\cos\theta - c)\widehat{v}_{0+\infty} = 0 \tag{43}$$

This is a complex quantity. Only two among the four unknown parameters are to be found, the two others being fixed. For an obvious physically sound reason, it is chosen to fix (α, θ). The solution procedure consists then of integrating Eqs. (35), (36), (41), and (42) with a fourth-order Runge–Kutta scheme, shooting from (c_r, c_i) until Eq. (43) is satisfied. When convergence is obtained, eigenvalues and eigenfunctions are found for the stability problem. The most unstable modes are characterized by the values of (α, θ) providing the maximum αc_i. In case of neutral modes, convergence cannot be reached by the present numerical procedure. The lowest value of the imaginary phase speed for which results are presented is typically $c_i \sim 0.005\Delta U/2$.

It is possible to derive a priori the pressure-perturbation behavior at infinity vs the freestream conditions: for unstable modes, $c_i > 0$ and $Z^{1/2} = A + jB$ with, as already mentioned, $A > 0$. Boundary conditions give

$$\widehat{p}_{0y\to-\infty} = \exp\{\alpha A y\}\exp\{j\alpha B y\}$$

$$\widehat{p}_{0y\to+\infty} = \exp\{-\alpha A y\}\exp\{-j\alpha B y\}$$

This is an acoustic wave, which is damped more quickly with higher A. On the other hand, for quasi-neutral modes, $c_i \approx 0$ and Z is real. In a subsonic mixing layer, $Z > 0$ and the pressure waves decay exponentially at infinity with no oscillations. If the mixing layer is supersonic enough for $(U_{\pm\infty}\cos\theta - c_r)$ to be greater than a, $Z < 0$, and writing $Z = j^2|Z|$, the solution of (37) behaves like

$$\widehat{p}_{0y\to\pm\infty} = \exp\left\{j\alpha|Z|^{\frac{1}{2}} y\right\} + \exp\left\{-j\alpha|Z|^{\frac{1}{2}} y\right\}$$

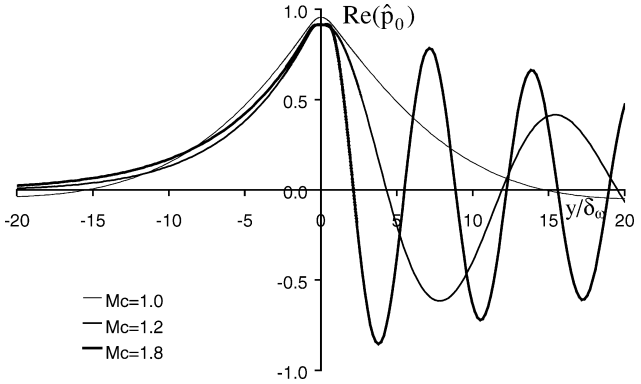

Fig. 3 Real part of $\widehat{p_0}$ in the isothermal O_2/N_2 mixing layer: $T = 300$ K, $\theta = 0$.

which is a pressure wave radiating undamped in the free stream (this is a key feature for noise pollution of supersonic shear flows). Figure 3 shows the pressure-perturbation amplitude in a plane isothermal $T = 300K$ O_2/N_2 mixing layer. Sound velocities are $a_{N_2} = 353$ m/s and $a_{O_2} = 330$ m/s. At $M_c = 1.8$, freestream conditions are $U_{\pm\infty} = \pm 614$ m/s. The most unstable mode given by the stability analysis is $\alpha\delta_\omega = 0.362$, which is a wavelength of $17.36\delta_\omega$, $c_r = -0.486U_\infty$, $c_i = 0.035U_\infty$. On the N_2 side ($y < 0$), $|U_{-\infty} - c_r| = 316$ m/s < 353 m/s and the wave is damped with no oscillations, whereas on the O_2 side ($y > 0$), $U_{+\infty} - c_r = 912$ m/s > 330 m/s and the wave oscillates with very low damping (αc_i is not strictly zero).

IV. Results

The main original results of this study are presented here. First, the range of wave numbers that are double-valued in phase speed is determined for plane modes of binary systems O_2/N_2 and O_2/H_2, generalizing therefore the previous results obtained for the compressible hyperbolic tangent mean flow. Second, the angle of propagation of perturbations is made variable from 0 to 90 deg and most unstable modes are determined at each angle for varying M_c. Hence, at a given M_c, the optimum angle of propagation to destabilize the mixing layer is found. An empirical model is then provided for the temporal stability of compressible binary mixing layers, assuming that the corresponding incompressible properties are known.

A. Double-Valued Solutions for Plane Modes

Blumen et al.[7] have shown that for the compressible temporal hyperbolic tangent velocity profile, unstable wavelengths exist in the range $M_c \in [1, \sqrt{2}]$ that are double-valued in imaginary phase speed c_i and show opposite real phase speeds c_r. The modes associated with negative c_r are the continuation of $M_c < 1$ steady modes and have higher c_i. The modes with positive c_r emerge from a stable state and are weakly amplified. We will call the former *primary* modes, and the latter *secondary* modes, not to be confused with modes associated with secondary instability.[25] Above $M_c = \sqrt{2}$, imaginary phase speeds merge and decrease continuously with further increases in M_c. The same holds qualitatively for binary mixing layers, but this time, nonunity density ratios produce nonopposite real phase speeds. In convectively unstable spatially developing compressible mixing layers, three modes of instability exist[16,19]: a central mode corresponding to our primary mode, and, at high enough compressibility or heat release (reacting case), two outer modes. In the case of temporal mixing layers, only one outer mode exists at high M_c, the secondary mode. Shin and Ferziger[18] invoke the symmetry of the problem as an explanation.

Figures 4 and 5 (see Sec. V.A for reference values) show the stability diagram of two-dimensional modes ($\theta = 0$) for the O_2/N_2 pair. As in the hyperbolic tangent case, three stages are to be distinguished with increasing M_c:

1) At low M_c, unstable wavelengths $2\pi/\alpha$ have single phase speeds but with nonzero quasi-constant positive real part (primary or "central" modes).

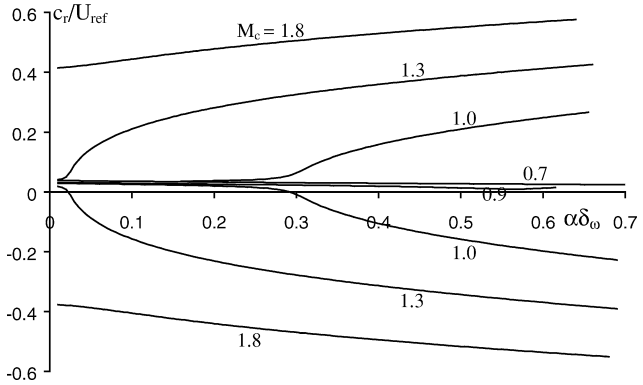

Fig. 4 Real phase speed for the O_2/N_2 isothermal mixing layer: $T = 300$ K, $\theta = 0$.

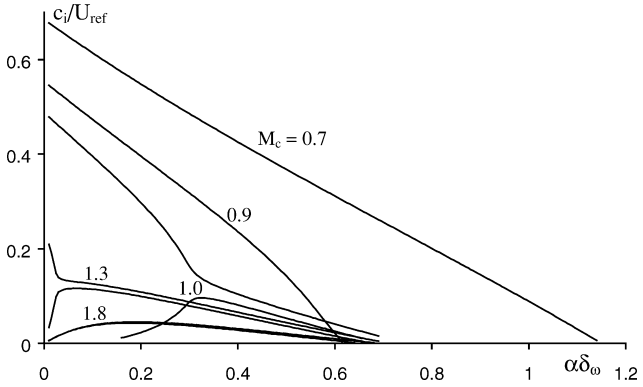

Fig. 5 Imaginary phase speed for the O_2/N_2 isothermal mixing layer: $T = 300$ K, $\theta = 0$.

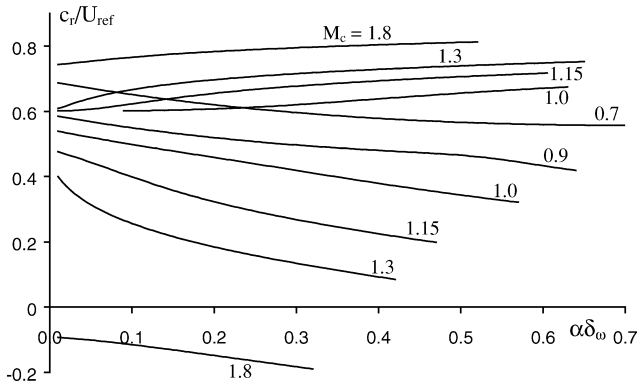

Fig. 6 Real phase speed for the O_2/H_2 isothermal mixing layer: $T = 300$ K, $\theta = 0$.

2) At $M_c \approx 0.92$, a range of unstable wavelengths emerge, whose phase speeds are double-valued with symmetric real parts around a low positive average value. The modes with lower c_r are the most amplified primary modes, whereas those with higher c_r are weakly amplified secondary modes (difficult to "catch" numerically).

3) Above $M_c \approx 1.8$, imaginary phase speeds merge and decrease with further increases in M_c.

The O_2/H_2 system shows the same sequence when M_c increases, but due to the higher density ratio, the secondary modes are very weakly amplified and we were unable to capture them numerically below $M_c = 0.95$ and above $M_c = 2$, the value at which they merge. The phase velocities c_r are no longer symmetric around a constant mean value. Their average is $\approx$ 10 to 20 times higher than in the low-density-ratio case over the range of existing unstable wavelengths and M_c (Figs. 6 and 7).

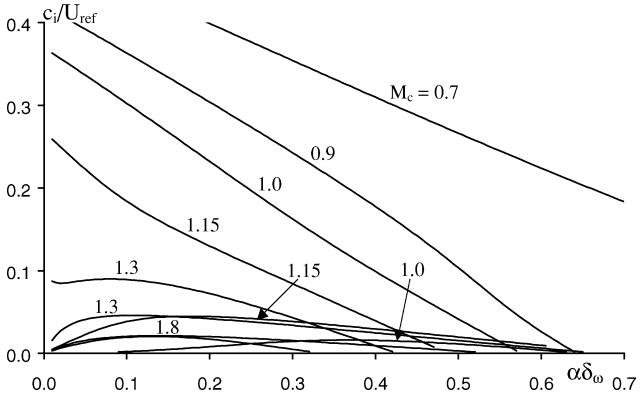

Fig. 7 Imaginary phase speed for the O_2/H_2 isothermal mixing layer: $T = 300$ K, $\theta = 0$.

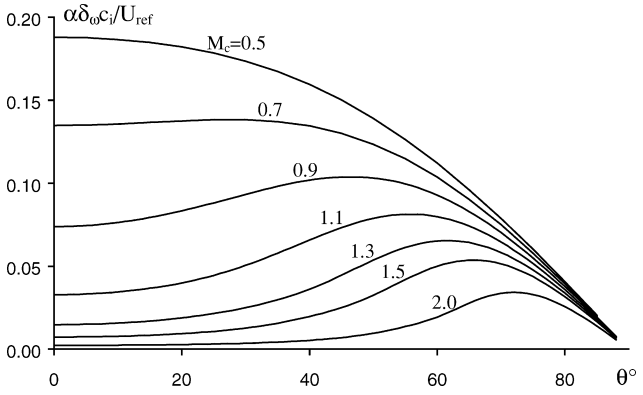

Fig. 8 Maximum amplification factor for the $T = 300$ K isothermal O_2/H_2 mixing layer vs θ for different M_c: primary modes.

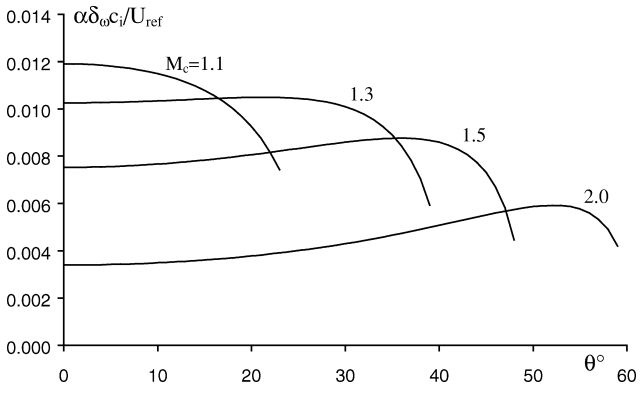

Fig. 9 Same as Fig. 8: secondary modes.

B. Most Amplified Modes vs θ (High-Density-Ratio Case)

We focus now on the O_2/H_2 pair and make θ variable. As in the plane case, at any given angle of propagation θ, unstable wavelengths exist, some of which are double-valued above $M_c \approx 0.95$. The most unstable wavelength is then determined for primary and secondary modes and corresponding phase velocities are computed. Figure 8 shows the amplification factor of the most amplified primary modes and Fig. 9 is the same for secondary modes.

At each value of M_c, the maximum observed defines the optimum propagation direction of perturbations to destabilize the mixing layer. As an example, for the O_2/H_2 system (Fig. 8), the optimal direction at $M_c = 1.1$ for primary modes is $\theta \approx 56$ deg. It is to be noticed that at a given convective Mach number, where the solution is double-valued, primary and secondary modes do not have the same optimum directions of propagation. To complete the results, Figs. 10 and 11 provide the corresponding real phase speeds and reduced wave numbers. These later increase with increasing θ whatever the

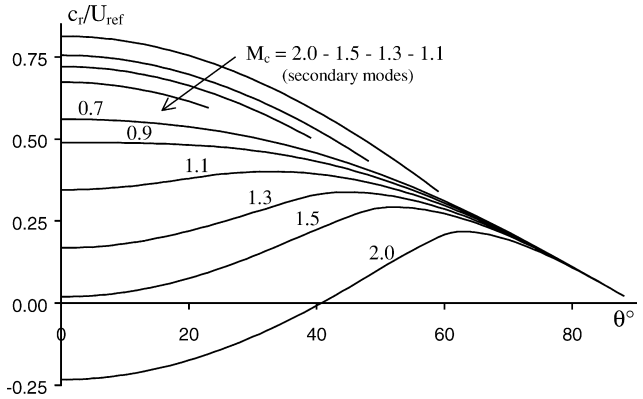

Fig. 10 Real phase speed of the most amplified primary and secondary modes vs θ for the $T = 300$ K isothermal O_2/H_2 mixing layer.

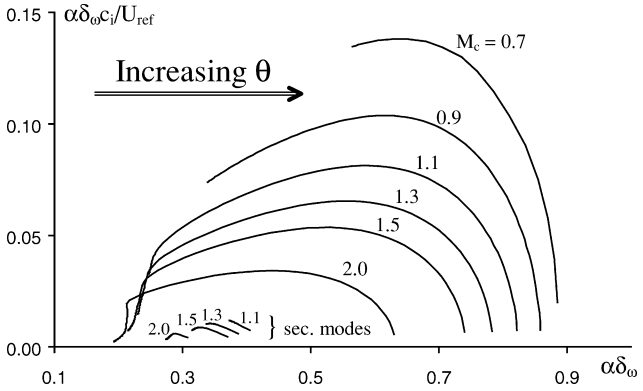

Fig. 11 Maximum amplification factor for the $T = 300$ K isothermal O_2/H_2 mixing layer vs α for different M_c.

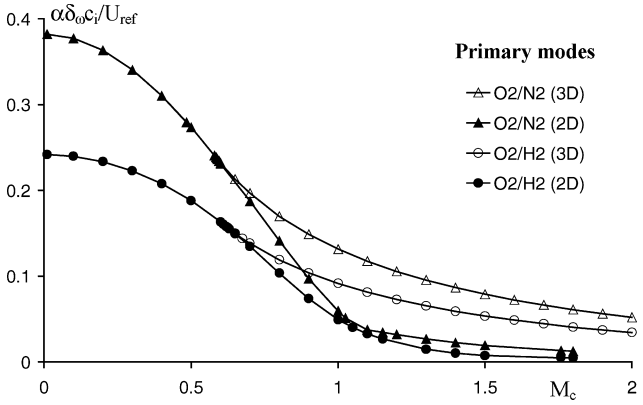

Fig. 12 Amplification factor of the most amplified two- and three-dimensional modes.

convective Mach number. The leftmost point of the curves is for $\theta = 0$ and the rightmost corresponds to the limit value of θ for which unstable modes exist. Primary modes have been found numerically up to 88 deg and extrapolation of the curves indicates that the angle $\theta = 90$ deg produces marginal amplification, that is, neutral modes. On the other hand, secondary modes only exist in a limited range of angles, increasing with the convective Mach number (Fig. 9).

C. Most Amplified Modes vs M_c

Three-dimensional effects are observed by comparison of the amplification factors of the most amplified plane modes ($\theta = 0$) to those of the most amplified three-dimensional modes. Figure 12 shows the result for the 300-K isothermal O_2/N_2 and O_2/H_2 mixing layers. Optimum angles of propagation for three-dimensional modes are reported in Fig. 13. Below $M_c \approx 0.6$, the most amplified modes

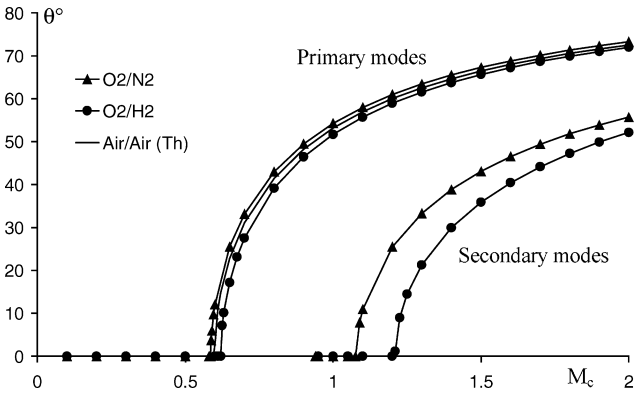

Fig. 13 Angle of propagation of the most amplified three-dimensional modes.

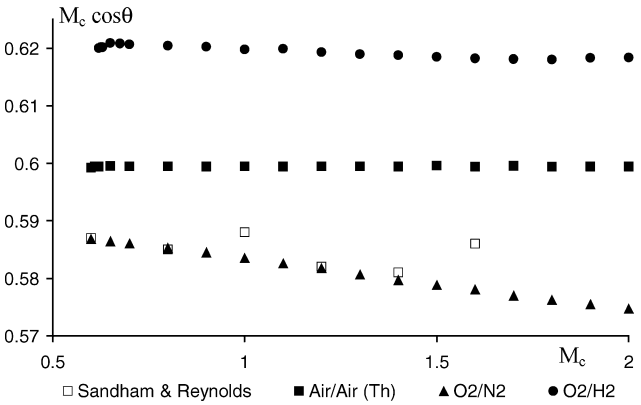

Fig. 14 $M_c \cos\theta$ for isothermal air/air (hyperbolic tangent), O_2/N_2, and O_2/H_2 temporal mixing layers, compared to the spatial monospecies case taken from Ref. 9.

are two-dimensional, and three-dimensional above. This is a well-known result for both spatially and temporally developing isothermal monospecies mixing layers.[9] Day et al. (Fig. 14 in Ref. 19) obtained the same results in the case of convective instability in the range $0.4 \le \rho_1/\rho_2 \le 2.5$, and the present study shows that it applies also to high-density-ratio binary systems with absolute instability and to secondary modes. Sandham and Reynolds have found (Table 2 in Ref. 9) that the rough approximation $M_c \cos\theta \approx 0.6$ holds for the most unstable modes of spatially developing monospecies mixing layers, as M_c increases. In fact, Fig. 14 shows that $M_c \cos\theta$ is slightly decreasing with increasing M_c for binary systems but is constant at 0.6 for the temporally developing monospecies mixing layer (hyperbolic tangent velocity profile and Busemann relation for the temperature). Nevertheless, it is remarkable that density ratios as high as 16 do not fundamentally alter this feature. The bifurcation-like behavior observed in Fig. 13 needs some comments: because it is common to both spatial monospecies and temporal binary stability analysis, it is linked neither to the particular shape of the mean flow-velocity profile, nor to the real or complex values of c and α, nor to the mean flow-density profile in Eq. (34). The convective Mach number effect in Eq. (34) occurs on the speed of sound via the mean flow temperature T_s, which roughly follows a Busemann relation. Hence, the temperature distribution in the shear layer is surely responsible for the abrupt change in θ at $M_c \approx 0.6$. Further research is needed to understand fully this point. Another interesting feature is the evolution of the most amplified wave numbers as M_c increases (Fig. 15). First, in the incompressible limit, no uniform trend can be found versus the density ratio. Then, once three-dimensional modes are reached, the most amplified wave numbers stay strictly constant in the unit-density-ratio case and decrease in the same way for the binary case, whatever the density ratio is. As in the spatial case,[16] increasing the density ratio from ≈ 1.15 (O_2/N_2) to ≈ 16 (O_2/H_2) drastically reduces the growth rate of perturbations

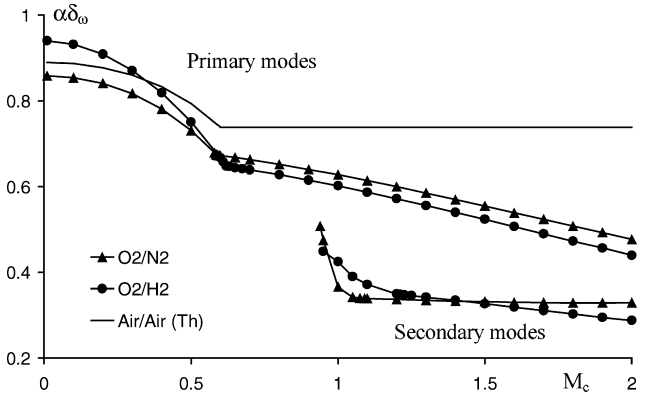

Fig. 15 Most amplified wave number for isothermal air/air, O_2/N_2, and O_2/H_2 temporal mixing layers.

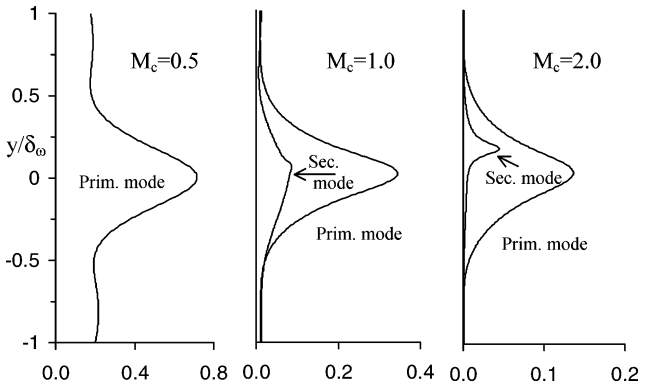

Fig. 16 Normalized vortical energy profiles [Eq. (44)]: O_2/N_2 system.

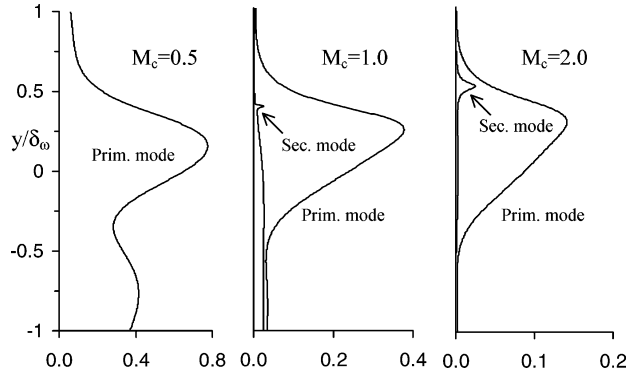

Fig. 17 Same as Fig. 16: O_2/H_2 system.

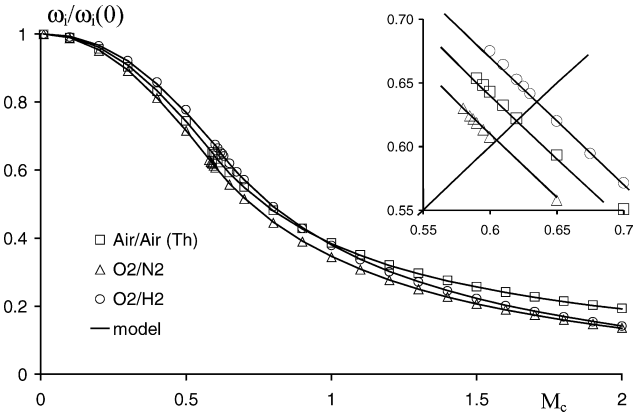

Fig. 18 Normalized peak amplification factor and model. Detail illustrates Eq. (45) and (46).

between 25 and 30% over the range of M_c considered. In Fig. 12, a sudden change in the slope of the two-dimensional O_2/N_2 curve is observed at $M_c \approx 1.1$. This corresponds to the transition from subsonic to supersonic phase speeds in the oxygen stream (see Fig. 3 and discussion at the end of Sec. III.B).

Numerical stability properties values for the O_2/N_2 and O_2/H_2 systems are gathered in tables given in the Appendix.

D. Eigenfunctions

Following Day et al.[19] the flow structure can be visualized thanks to the scaled eigenfunctions energy profile

$$\Psi = \frac{\omega_i(M_c)_{\max}}{\omega_i(0)_{\max}}\left(|\widehat{u_0}|^2 + |\widehat{v_0}|^2 + |\widehat{w_0}|^2\right) \tag{44}$$

where $\omega_i = \alpha c_i$. In reference to Sec. IV.E, the maximum amplification observed at M_c for a given system of gases is normalized by the corresponding incompressible value, rather than the monospecies incompressible one. Figures 16 and 17 display the Ψ profiles for the O_2/N_2 and O_2/H_2 systems, respectively, at $M_c = 0.5$, 1.0, and 2.0. Compressibily effects are very similar in the near-unity density-ratio case, and vortical energy profiles compare very well to those of the spatial case, although the scaling is not the exactly the same, both in shape and in amplitude. As in the spatial case, increasing the density ratio causes a shift of both primary and secondary modes toward the heavy gas side, whatever the convective Mach number. It is not obvious, however, which one of the fast or slow spatial outer modes could be identified with the single temporal secondary mode, because fast/slow and heavy/light combinations cannot be reproduced in the temporal mixing layer, and this question probably does not make sense. The mixing efficiency that results from the vortical energy distribution is discussed in detail in Ref. 19.

E. Empirical Modeling of the Results

Previous studies have shown that normalization of compressible mixing layer peak amplification factors by the corresponding incompressible ($M_c = 0$) value produces some uniform trend (although Fig. 10 in Ref. 16 is different from Fig. 5 in Ref. 9 and Fig. 3 in Ref. 26, the latter two being identical) whatever the density ratio is; thus results at a given M_c can be predicted if the incompressible value is known. Nevertheless, except in Ref. 27 for the growth rate of spatial mixing layers, no explicit fit is given in the literature. An attempt is made here to fill this gap.

Two physical parameters are at our disposal to build an empirical model: the density ratio $\beta_\rho = \rho_1/\rho_2$ and the convective Mach number of bifurcation from two-dimensional to three-dimensional modes (Fig. 13), denoted hereafter by M^*. Because this value separates the range of M_c into two parts, the model is built independently for $0 \le M_c \le M^*$ (two-dimensional modes) and for $M^* \le M_c$ (three-dimensional modes). First, the normalized amplification factor $\omega_i(M_c)/\omega_i(0)$ has the remarkable property (Fig. 18) that

$$\frac{\omega_i(M^* + 0.02)}{\omega_i(0)} = M^* + 0.02, \qquad \frac{1}{\omega_i(0)}\frac{\partial \omega_i}{\partial M_c}(M^* + 0.02) = -1 \tag{45}$$

both for O_2/N_2 and O_2/H_2 but also for the monospecies hyperbolic tangent case. Values of M^* for these cases are, respectively, 0.585, 0.62, and 0.6. Hence, we deduce that

$$\omega_i(M^*)\big/\omega_i(0) \approx M^* + 0.04 \tag{46}$$

For $0 \le M_c \le M^*$, a nice fit is obtained with the expression

$$\frac{\omega_i^{(2D)}(M_c)}{\omega_i(0)} = \exp\left\{(7.6666(M^* + 0.02) - 6.1183)M_c^{3.55(M^* + 0.02)}\right\} \tag{47}$$

which is coherent with relation (46) under a 1% error for $0.54 \le M^* \le 0.63$. The normalized wave number at M^* (Fig. 19) shows no straightforward relation with the density ratio β_ρ, and if a

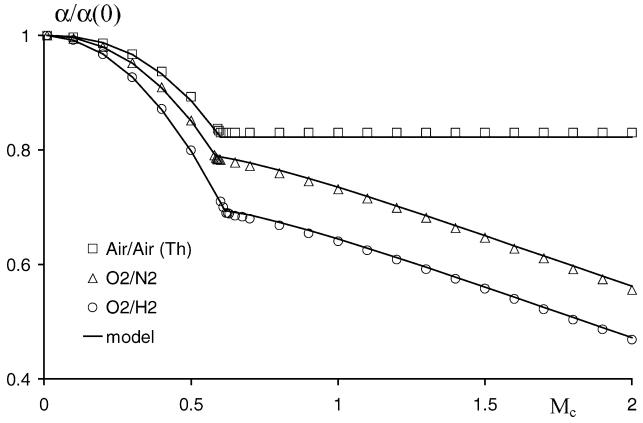

Fig. 19 Normalized most unstable wave number and model.

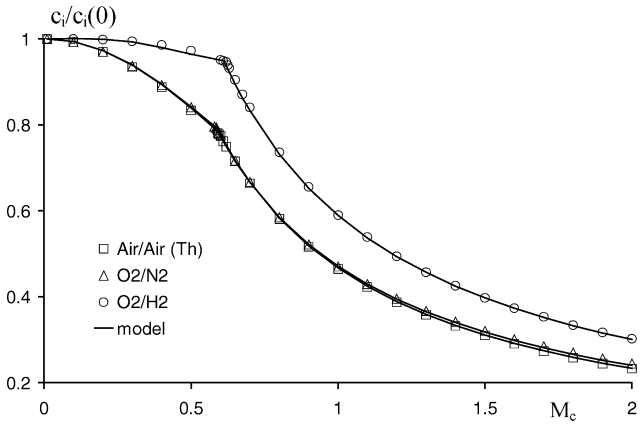

Fig. 20 Normalized imaginary phase speed of the most unstable wave number and model.

power law is assumed for two-dimensional modes, the best fit is

$$\frac{\alpha^{(2D)}(M_c)}{\alpha(0)} = 1 - aM_c{}^n \tag{48}$$

with the constant a taking the proper value to reach $\alpha(M^*)/\alpha(0)$ at M^*, and the exponent n slightly decreasing with β_ρ. A good fit is

$$n = 2 + 0.4/\beta_\rho^5 \tag{49}$$

The normalized imaginary phase speed at M^* (Fig. 20) clearly indicates the relevant parameter to be the density ratio β_ρ, and we find the fit

$$c_i(M^*)/c_i(0) = 1 - 0.222/\sqrt{\beta_\rho} \tag{50}$$

This relation combined with relation (46) gives the value of $\alpha(M^*)/\alpha(0)$ to compute the constant a in Eq. (48), and one can then complete the two-dimensional model with

$$\frac{c_i^{(2D)}(M_c)}{c_i(0)} = \frac{\omega_i^{(2D)}(M_c)}{\omega_i(0)} \frac{\alpha(0)}{\alpha^{(2D)}(M_c)} \tag{51}$$

Above M^*, the most amplified wave numbers are strictly constant for the symmetric monospecies mean flow with value $\alpha(M^*)/\alpha(0)$ and decrease exactly the same way from this value in the O_2/N_2 and O_2/H_2 cases:

$$\frac{\alpha^{(3D)}(M_c)}{\alpha(0)} = \frac{\alpha(M^*)}{\alpha(0)} - \left\{1 - \exp\left[-0.1666\left(M_c - M^*\right)^{1.25}\right]\right\} \tag{52}$$

Finally, the imaginary phase speed follows the simple law for binary systems

$$\frac{c_i^{(3D)}(M_c)}{c_i(0)} = \frac{c_i(M^*)}{c_i(0)} \left(\frac{M^*}{M_c}\right)^{0.97} \tag{53}$$

the exponent 0.97 turning to 1.00 in the hyperbolic tangent case. The model for the maximum three-dimensional amplification factor follows from Eqs. (52) and (53), and the model for $c_r(M_c)/c_r(0)$ is the same as the one for $c_i(M_c)/c_i(0)$.

The main shortcoming of this model is the unknown value of M^*, but taking the mean value $M^* = 0.6$ gives results that are under 5% error, even in a heated flow, and density ratios as high as 32. Results of the model applied to various test cases are given in Table 1.

V. Direct Numerical Simulation

The issue addressed in this section is the performance of the linear inviscid stability theory extended to high-density-ratio compressible binary mixing layers by comparing the predicted growth rates and phase velocities to those computed in direct numerical simulations.

A. Direct Numerical Simulation Code

Calculations are made in dimensionless variables. Reference values are

$$\begin{aligned}
\text{velocity}: &\quad U_{\text{ref}} = \Delta U/2 \\
\text{length}: &\quad L_{\text{ref}} = \delta_0 = \delta_\omega(t=0) \\
\text{time}: &\quad t_{\text{ref}} = L_{\text{ref}}/U_{\text{ref}} \\
\text{temperature}: &\quad T_{\text{ref}} = (T_1 + T_2)/2 \\
\text{density}: &\quad \rho_{\text{ref}} = P/0.5(r_1 + r_2)/T_{\text{ref}} \\
\text{pressure}: &\quad P_{\text{ref}} = \rho_{\text{ref}} * U_{\text{ref}}^2 \\
\text{viscosity}: &\quad \mu_{\text{ref}} = \mu(T_{\text{ref}}, Y = 0.5)
\end{aligned}$$

Navier–Stokes equations (5–8) are solved in convective form for primitive variables ρ, u, v, w, T, Y because this form reduces numerical aliasing errors and leads to a simpler formulation of boundary conditions.[28] Spatial discretization is achieved by a sixth-order centered compact finite difference scheme[29] in the homogeneous direction and in the interior domain, and a fourth-order one-sided compact scheme at the nonperiodic upper and lower boundary nodes and their immediate neighbors. A third-order, low-storage Runge–Kutta scheme[30] is used for time stepping. Periodic boundary conditions are applied in the homogeneous directions and nonreflective conditions[31] at freestream boundaries (Fig. 21).

B. Test Cases and Procedure

Six test cases are examined, whose physical characteristics and theoretical stability properties are summarized in Table 1. Cases 1–5 have low M_c, so the most unstable modes are plane modes ($\theta = 0$), whereas case 6 has a three-dimensional ($\theta = 55.7$ deg) most unstable mode. Comparisons of test cases make it possible to isolate the following effects: 1) 1 and 4, density ratio at the same M_c (isothermal

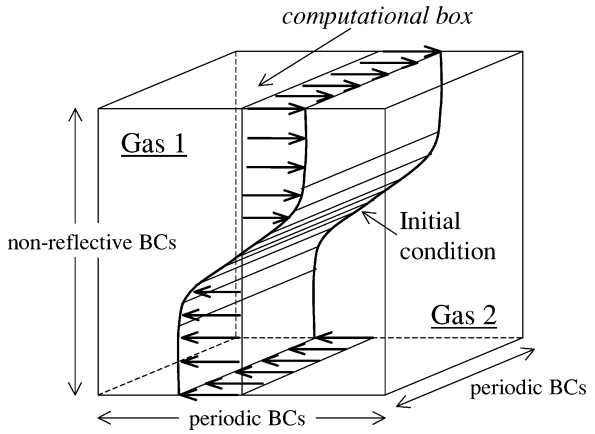

Fig. 21 Computational box for temporal DNS.

Table 1 Physical characteristics and stability properties (inviscid linear theory) for DNS test cases[a]

	Value for case and species:					
Parameter	1, O_2/N_2	2, O_2/N_2	3, O_2/H_2	4, O_2/H_2	5, O_2/H_2	6, O_2/H_2
$\Delta U/2$	166 m/s	228 m/s	400 m/s	400 m/s	400 m/s	906.3
T_1/T_2, K	300/300	200/1389	600/300	300/300	300/600	300/300
ρ_1/ρ_2	1.143	7.937	7.937	15.87	31.75	15.87
M_c	0.485	0.450	0.450	0.485	0.366	1.100
αL_{ref}	0.739	0.932	0.785	0.761	0.787	0.587
	(+2.2)	(−6.5)	(−3.6)	(−2.5)	(+0.1)	(−2.4)
c_r/U_{ref}	0.028	0.610	0.479	0.605	0.718	0.327
	(+2.1)	(+0.3)	(+2.1)	(+1.3)	(+0.4)	(+2.4)
c_i/U_{ref}	0.378	0.256	0.302	0.251	0.202	0.138
	(+1.3)	(+2.7)	(+1.0)	(−1.6)	(−3.0)	(−2.2)
$\alpha c_i t_{\text{ref}}$	0.279	0.239	0.237	0.191	0.159	0.0813
	(+3.6)	(−4.2)	(−2.5)	(−4.2)	(−3.1)	(−4.8)

[a]Values in parentheses are % errors for the model of Sec. IV.E with $M^* = 0.6$ fixed in each case.

cases); 2) 4 and 6, M_c at the same density ratio; 3) 2 and 3, speed of sound in the freestreams at the same M_c and density ratio; and 4) 3 and 5, density ratio through temperature of the freestreams.

The corresponding eigenfunctions are superposed on the mean flow as initial conditions for the direct numerical simulation (DNS). Their amplitudes are scaled so that

$$\max_y\{|\widehat{u_0}|\} = 0.05\Delta U/2$$

In each two-dimensional case, the length of the computational box corresponds to one wavelength of the most unstable mode. In case 6, periodicity of boundary conditions in the streamwise and spanwise directions imposes $L_x = 2\pi/\alpha\cos\theta$ and $L_z = 2\pi/\alpha\sin\theta$. Hence, a single simulated vortex emerges from the early Kelvin–Helmholtz instability. The questions to be answered are as follows: 1) Does the velocity of traveling eddies observed in the DNS corresponds to the predicted real phase speed? 2) Does the growth rate of the fluctuating kinetic energy correspond to the predicted amplification factor? 3) What is the influence of viscous effects (Reynolds number in the simulations) on the agreement with the linear inviscid theory?

The time growth rate of the fluctuating kinetic energy is evaluated in the following way: the mean value in the homogeneous (x, z) plane of any field $\phi(x, y, z, t)$ is defined at transverse coordinate y and time t as

$$\bar{\phi}(y, t) = \frac{1}{L_x L_z}\int_0^{L_x}\int_0^{L_z}\phi(x, y, z, t)\,\mathrm{d}x\,\mathrm{d}z$$

and its fluctuating part as

$$\phi'(x, y, z, t) = \phi(x, y, z, t) - \bar{\phi}(y, t)$$

The fluctuating kinetic energy is then

$$k(t) = \int_0^{L_x}\int_0^{L_y}\int_0^{L_z}\Big(u'^2(x, y, z, t) + v'^2(x, y, z, t) + w'^2(x, y, z, t)\Big)\,\mathrm{d}x\,\mathrm{d}y\,\mathrm{d}z$$

From Eq. (26), we have

$$\frac{\partial u'}{\partial t} = \alpha c_i u'$$

$$\ell_n u' = \alpha c_i t + cst$$

Hence, the curve $\frac{1}{2}\ell_n[k(t)]$ should theoretically be linear at the beginning of the simulation, with slope αc_i.

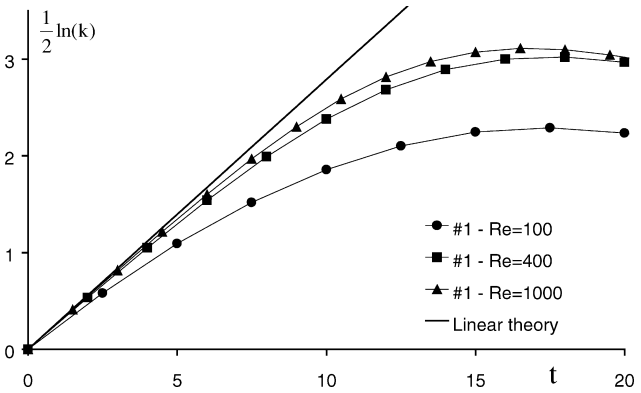

Fig. 22 Reynolds number effect on the temporal growth rate of kinetic energy for case 1.

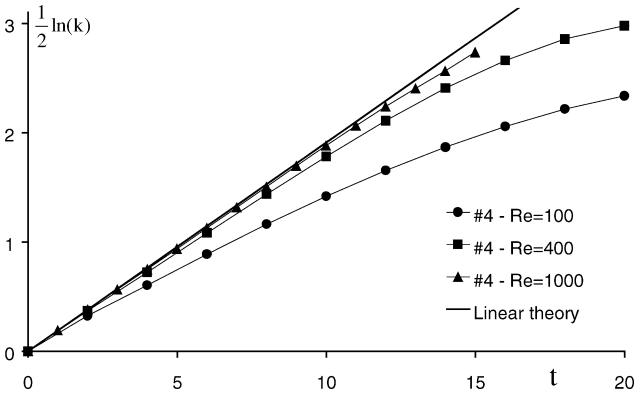

Fig. 23 Same as Fig. 22, case 4.

C. Results

1. Viscous Effects

The theory being inviscid, the influence of the Reynolds number is first investigated for cases 1 and 4. The Reynolds number based on reference length, velocity, and viscosity is made variable by changing the value of the initial vorticity thickness of the shear layer. For each case, three values are tested: 100, 400, and 1000. Figures 22 and 23 point out that a Reynolds number of at least 400 is necessary to allow comparison with the inviscid theory. Furthermore, the lower the amplification factor is, the longer DNS results match linear theory. In each case, the computed growth rate is lower than the predicted one because viscosity has a stabilizing effect by increasing diffusively the thickness of the shear region. The numerical saturation of the temporal box limits the amplification of perturbations, too (Ref. 6, p. 519).

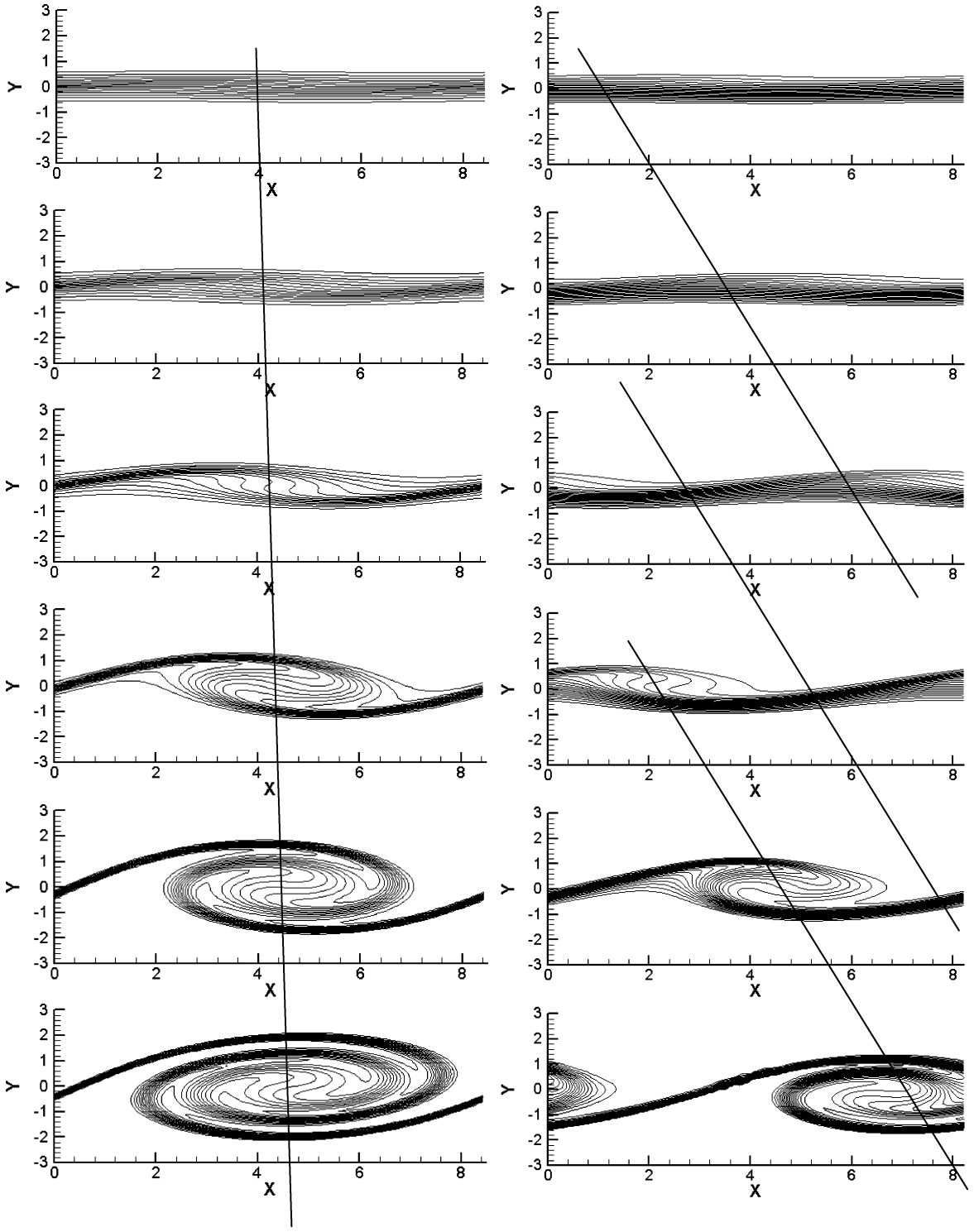

Fig. 24 Oxygen mass fraction. Left: 1, right: 4, $Re = 400$, at times $t = 0, 4, 8, 12, 16, 20$ (from top to bottom). Slope of oblique straight lines is theoretical real phase velocity.

2. Real Phase Speed

Figure 24 shows the oxygen mass fraction for cases 1 and 4. The theoretical real phase speeds are shown by oblique lines of corresponding slope. The velocity of traveling eddies coincides visually very well with the predicted values (Table 1) because this feature is independent of viscous effects and the numerical scheme has very low dispersive error. The growth rates are also apparent. Figure 25 shows the surface of isovalue $Y_{O_2} = 0.5$ at time $t = 0$, 10, 20, and 30 for case 6. The direction of propagation of the perturbation (horizontal on the paper view) is exactly the predicted value, and once again, the real phase speed is well predicted. To our knowledge, this has never been checked in previous studies.

3. Growth Rates

It has been shown (Sec. IV.C, Fig. 12) that increasing both convective Mach number and density ratio reduces the amplification factor predicted by the linear theory. To modify the density ratio, one can change the gases under isothermal conditions or change the temperature of the freestreams for a given pair of gases. Modifying the temperature distribution also changes the value of M_c, which is,

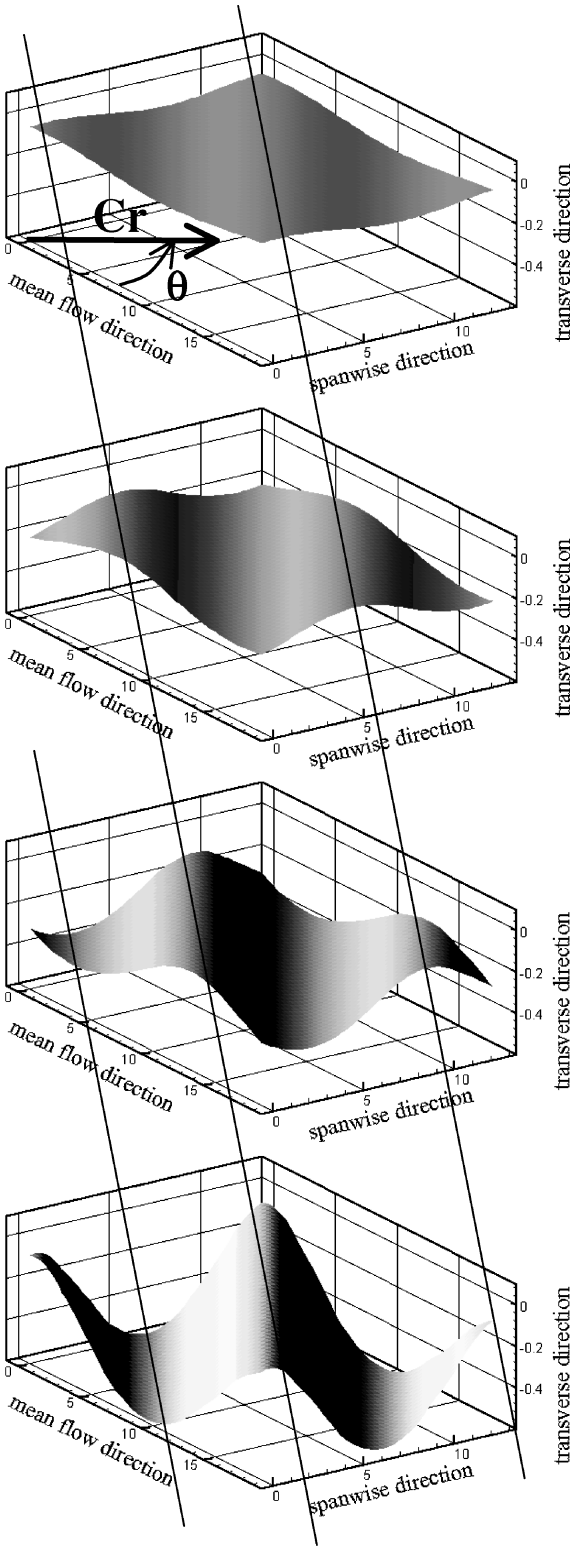

Fig. 25 Isosurface $Y = 0.5$ at time $t = 0, 10, 20, 30$ (from top to bottom), case 6: $Re = 400$. The view vector is in the plane normal to the direction of propagation.

moreover, linearly dependent on the freestreams velocity difference. The change in density ratio at constant M_c has been illustrated in Figs. 22 and 23.

Temperature effects are investigated by comparison of cases 3 and 5 at $Re = 400$ (Fig. 26). Decreasing the density ratio by heating the oxygen stream reduces the time interval where linear theory and DNS results match. The opposite effect is obtained by heating the hydrogen stream. In this latter case, the agreement is excellent.

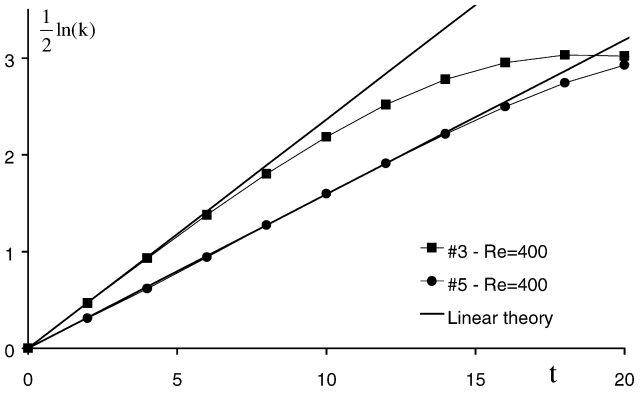

Fig. 26 Heating effect on the temporal growth rate of kinetic energy: cases 3 and 5, $Re = 400$.

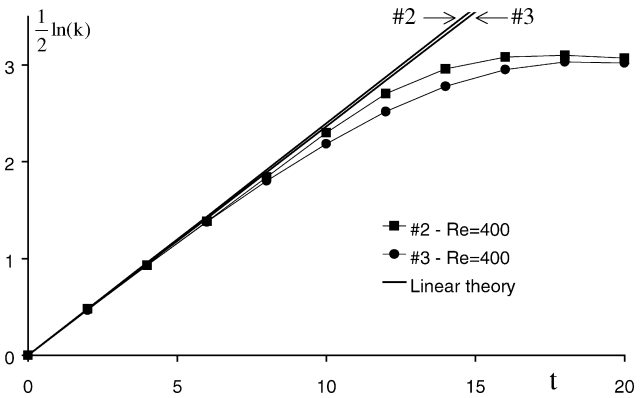

Fig. 27 Temporal growth rate of kinetic energy at the same M_c and density ratio for two different pairs of gases: cases 2 and 3, $Re = 400$.

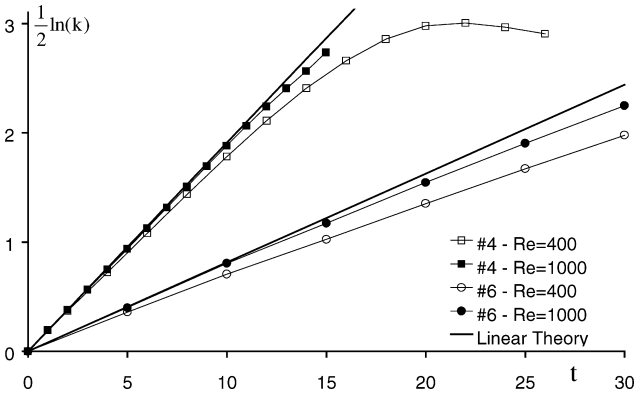

Fig. 28 Convective Mach number effect on the temporal growth rate of kinetic energy: cases 4 and 6, $Re = 400$ and 1000.

Cases 2 and 3 have been designed to have the same density ratio and M_c, although the gases are different. The linear theory predicts quite the same amplification factors, but different real phase speeds and more amplified wavelengths. DNS results reproduce these features closely (Fig. 27). Hence, extension of the stability theory to binary systems is useful to avoid erroneous conclusions deduced from monospecies theory, as mentioned by Lu and Lele.[26]

Finally, the prediction of convective Mach number effects at constant density ratio is compared to DNS results for cases 4 and 6 at $Re = 400$ and 1000. The former has a two-dimensional most unstable mode and the latter a three-dimensional. Although the same good qualitative agreement is observed in Fig. 28, one could have expected a better agreement in the three-dimensional case, due to the low amplification factor associated with the high M_c value. Nevertheless, increasing the Reynolds number for case 6 improves

the agreement with the predicted value. This means that viscous effects are more important for three-dimensional modes than for two-dimensional. One reason is the higher dilatation at higher M_c associated with the $-\frac{2}{3}$ constant in Eq. (9) changed to -1 in two-dimensional calculations.

VI. Conclusions

The temporal-stability properties of three-dimensional compressible binary shear layers have been investigated. The main feature associated with increasing the convective Mach number is the abrupt change in the direction of propagation of the most unstable modes above $M_c \approx 0.6$, nearly independent of the density ratio. Secondary unstable modes have been found in the range $\approx 1 < M_c < \approx 2$, weakly amplified but with nonopposite real phase speed, as is the case in monospecies mixing layers. The particularity of binary systems is that a great number of combinations in species, temperature distribution, and freestream velocities are allowed to vary the density ratio and the convective Mach number. Considering two extreme cases such as O_2/N_2 and O_2/H_2 at the same density ratio and M_c, one finds nearly the same maximum amplification factor but different most amplified wavelengths and real phase speeds. An empirical model has been proposed that allows to predict the stability properties of various flows within 5% error if incompressible values are known. Direct numerical simulations have confirmed the results of the inviscid linear stability theory extended to high-density-ratio binary mixing layers. Increasing both the density ratio and the convective Mach number makes the shear layer so stable that transition to turbulence in direct numerical simulations is nearly impossible unless the eigenfunctions of the stability problem are used as perturbations to bypass transition. Otherwise, the CPU time needed makes such calculation prohibitively expensive. In this sense, the linear inviscid stability theory is very useful and provides quite accurate predictions in the temporal growth rate of the shear layer if the associated Reynolds number is greater than 400. Phase velocities and directions of propagation are always well predicted.

Appendix: Temporal Stability Properties of O_2/H_2 and O_2/N_2 Systems: Numerical Values

Table A1 Most amplified primary modes for the isothermal $T = 300$ K O_2/H_2 system

M_c	θ°	$\alpha\delta_\omega$	c_r/U_{ref}	$\alpha\delta_\omega c_i/U_{\text{ref}}$
0.01	0	0.940	0.639	0.2418
0.1	0	0.932	0.638	0.2397
0.2	0	0.909	0.634	0.2334
0.3	0	0.871	0.627	0.2228
0.4	0	0.819	0.616	0.2077
0.5	0	0.751	0.602	0.1880
0.6	0	0.667	0.584	0.1633
0.61	0	0.658	0.582	0.1606
0.62	0.021	0.648	0.580	0.1578
0.625	7.150	0.648	0.576	0.1565
0.63	10.15	0.647	0.571	0.1551
0.65	17.21	0.644	0.554	0.1499
0.675	23.12	0.642	0.533	0.1438
0.7	27.55	0.639	0.514	0.1382
0.8	39.15	0.628	0.450	0.1189
0.9	46.44	0.615	0.400	0.1037
1.0	51.70	0.602	0.360	0.0914
1.1	55.70	0.587	0.327	0.0813
1.2	58.93	0.572	0.299	0.0727
1.3	61.57	0.556	0.276	0.0654
1.4	63.77	0.540	0.256	0.0591
1.5	65.65	0.524	0.239	0.0536
1.6	67.27	0.507	0.224	0.0487
1.7	68.68	0.490	0.211	0.0445
1.8	69.92	0.473	0.199	0.0406
1.9	71.01	0.457	0.189	0.0372
2.0	71.99	0.440	0.179	0.0342

Table A2 Most amplified secondary modes for the isothermal $T = 300$ K O_2/H_2 system

M_c	θ°	$\alpha\delta_\omega$	c_r/U_{ref}	$\alpha\delta_\omega c_i/U_{\text{ref}}$
0.95	0	0.449	0.590	0.0015
1.0	0	0.425	0.643	0.0064
1.05	0	0.390	0.659	0.0108
1.1	0	0.372	0.674	0.0119
1.2	0	0.350	0.699	0.0115
1.21	1.17	0.349	0.702	0.0114
1.225	8.93	0.348	0.693	0.0112
1.25	14.44	0.346	0.680	0.0110
1.3	21.28	0.342	0.655	0.0105
1.4	29.94	0.335	0.610	0.0095
1.5	35.90	0.327	0.571	0.0087
1.6	40.47	0.319	0.537	0.0080
1.7	44.17	0.311	0.507	0.0074
1.8	47.25	0.303	0.481	0.0069
1.9	49.88	0.295	0.458	0.0064
2.0	52.16	0.288	0.437	0.0059

Table A3 Most amplified primary modes for the isothermal $T = 300$ K O_2/N_2 system

M_c	θ°	$\alpha\delta_\omega$	c_r/U_{ref}	$\alpha\delta_\omega c_i/U_{\text{ref}}$
0.01	0	0.859	0.0332	0.3820
0.1	0	0.854	0.0330	0.3773
0.2	0	0.841	0.0323	0.3632
0.3	0	0.817	0.0313	0.3405
0.4	0	0.781	0.0300	0.3102
0.5	0	0.731	0.0285	0.2735
0.585	0	0.675	0.0272	0.2384
0.59	5.93	0.673	0.0270	0.2363
0.6	12.04	0.672	0.0266	0.2321
0.65	25.55	0.668	0.0245	0.2131
0.7	33.15	0.663	0.0227	0.1967
0.8	42.98	0.652	0.0199	0.1698
0.9	49.50	0.640	0.0176	0.1487
1.0	54.30	0.628	0.0159	0.1316
1.1	58.02	0.614	0.0144	0.1175
1.2	61.00	0.600	0.0132	0.1056
1.3	63.47	0.585	0.0122	0.0955
1.4	65.54	0.570	0.0114	0.0867
1.5	67.30	0.555	0.0106	0.0791
1.6	68.82	0.539	0.0100	0.0723
1.7	70.16	0.524	0.0095	0.0664
1.8	71.33	0.508	0.0090	0.0611
1.9	72.37	0.493	0.0086	0.0563
2.0	73.30	0.477	0.0082	0.0520

Table A4 Most amplified secondary modes for the isothermal $T = 300$ K O_2/N_2 system

M_c	θ°	$\alpha\delta_\omega$	c_r/U_{ref}	$\alpha\delta_\omega c_i/U_{\text{ref}}$
0.94	0	0.508	0.152	0.0149
0.95	0	0.475	0.143	0.0202
1.0	0	0.366	0.140	0.0329
1.05	0	0.342	0.184	0.0338
1.09	7.87	0.339	0.207	0.0327
1.1	10.95	0.339	0.206	0.0324
1.2	25.51	0.337	0.195	0.0295
1.3	33.30	0.335	0.186	0.0271
1.4	38.83	0.333	0.180	0.0250
1.5	43.11	0.332	0.174	0.0232
1.6	46.56	0.330	0.170	0.0217
1.7	49.42	0.330	0.167	0.0203
1.8	51.84	0.330	0.165	0.0191
1.9	53.91	0.330	0.163	0.0180
2.0	55.70	0.330	0.162	0.0170

Acknowledgment

We thank the French computing center Institut du Développement et des Ressources en Informatique Scientifique for providing computational resources on the NEC SX5 supercomputer.

References

[1]Gutmark, E. J., Schadow, K. C., and Yu, K. H., "Mixing Enhancement in Supersonic Free Shear Flows," *Annual Review of Fluid Mechanics*, Vol. 27, 1995, pp. 375–417.

[2]Betchov, R., and Criminale, W. O., *Stability of Parallel Flows*, Vol. 10, Applied Mathematics and Mechanics, Academic Press, New York, 1967.

[3]Michalke, A., "On the Inviscid Stability of the Hyperbolic Tangent Velocity Profile," *Journal of Fluid Mechanics*, Vol. 19, Pt. 3, 1964, pp. 543–556.

[4]Michalke, A., "On Spatially Growing Disturbances in an Inviscid Shear Layer," *Journal of Fluid Mechanics*, Vol. 23, Pt. 3, 1965, pp. 521–544.

[5]Comte, P., Lesieur, M., Laroche, H., and Normand, X., "Numerical Simulation of Plane Shear Layers," *Turbulent Shear Flows*, Vol. 6, edited by J.-C. André, J. Cousteix, F. Durst, B. E. Launder, F. W. Schmidt, and J. H. Whitelaw, Springer-Verlag, Berlin, 1989, pp. 360–380.

[6]Lesieur, M., Staquet, C., Le Roy, P., and Compte, P., "The Mixing Layer and Its Coherence Examined from the Point of View of Two Dimensional Turbulence," *Journal of Fluid Mechanics*, Vol. 192, 1988, pp. 511–534.

[7]Blumen, W., Drazin, P. G., and Billings, D. F., "Shear Layer Instability of an Inviscid Compressible Fluid. Part 2," *Journal of Fluid Mechanics*, Vol. 71, Pt. 2, 1975, pp. 305–316.

[8]Balsa, T. F., and Goldstein, M. E., "On the Stability of Supersonic Mixing Layers: A High-Mach-Number Asymptotic Theory," *Journal of Fluid Mechanics*, Vol. 216, 1990, pp. 585–611.

[9]Sandham, N. D., and Reynolds, W. C., "Compressible Mixing Layer: Linear Theory and Direct Simulation," *AIAA Journal*, Vol. 28, No. 4, 1990, pp. 618–624.

[10]Brown, G. L., and Roshko, A., "On Density Effects and Large Structure in Turbulent Mixing Layers," *Journal of Fluid Mechanics*, Vol. 64, Pt. 4, 1974, pp. 775–816.

[11]Jackson, T. L., and Grosch, C. E., "The Inviscid Spatial Stability of a Compressible Mixing Layer," *Journal of Fluid Mechanics*, Vol. 208, 1989, pp. 609–637.

[12]Jackson, T. L., and Grosch, C. E., "The Inviscid Stability of a Compressible Mixing Layer. Part III. Effects of Thermodynamics," *Journal of Fluid Mechanics*, Vol. 224, 1991, pp. 159–175.

[13]Grosch, C. E., and Jackson, T. L., "Inviscid Spatial Stability of a Three-Dimensional Compressible Mixing Layer," *Journal of Fluid Mechanics*, Vol. 231, 1991, pp. 35–50.

[14]Jackson, T. L., and Grosch, C. E., "Absolute/Convective Instabilities and the Convective Mach Number in a Compressible Mixing Layer," *Physics of Fluids*, Vol. 2, No. 6, 1990, pp. 949–954.

[15]Dutton, C., "Compressible Turbulent Free Shear Layers," *AGARD Report—Turbulence in Compressible Flows*, R-819, 1997, pp. 2-1–2-42.

[16]Kozusko, F., Lasseigne, D. G., Grosch, C. E., and Jackson, T. L., "The Stability of Compressible Mixing Layers in Binary Gases," *Physics of Fluids*, Vol. 8, No. 7, 1996, pp. 1954–1963.

[17]Kozusko, F., Grosch, C. E., Jackson, T. L., Kennedy, C. A., and Gatski, T. B., "The Structure of Variable Property, Compressible Mixing Layers in Binary Gas Mixtures," *Physics of Fluids*, Vol. 8, No. 7, 1996, pp. 1945–1953.

[18]Shin, D. S., and Ferziger, J. H., "Linear Stability of the Reacting Mixing Layer," *AIAA Journal*, Vol. 29, No. 10, 1991, pp. 1634–1642.

[19]Day, M. J., Reynolds, W. C., and Mansour, N. N., "The Structure of the Compressible Reacting Mixing Layer: Insights from Linear Stability Analysis," *Physics of Fluids*, Vol. 10, No. 4, 1998, pp. 993–1007.

[20]Papamoschou, D., and Roshko, A., "The Compressible Turbulent Shear Layer: An Experimental Study," *Journal of Fluid Mechanics*, Vol. 197, 1988, pp. 453–477.

[21]Huerre, P., and Monkewitz, P. A., "Absolute and Convective Instabilities in Free Shear Layers," *Journal of Fluid Mechanics*, Vol. 159, 1985, pp. 151–168.

[22]Pavithran, S., and Redekopp, L. G., "The Absolute-Convective Transition in Subsonic Mixing Layers," *Physics of Fluids A*, Vol. 1, No. 10, 1989, pp. 1736–1739.

[23]Strykowski, P. J., and Niccum, D. L., "The Influence of Velocity and Density Ratio on the Dynamics of Spatially Developing Mixing Layers," *Physics of Fluids A*, Vol. 4, No. 4, 1992, pp. 770–781.

[24]Lardjane, N., Fedioun, I., and Gökalp, I., "Accurate Initial Conditions for the Direct Numerical Simulation of Temporal Compressible Binary Shear Layers with High Density Ratio," *Computers and Fluids Journal*, Vol. 33, No. 4, 2004, pp. 549–576.

[25]Metcalfe, R. W., Orszag, S. A., Brachet, M. E., Menon, S., and Riley, J. J., "Secondary Instability of a Temporally Growing Mixing Layer," *Journal of Fluid Mechanics*, Vol. 184, 1987, pp. 207–243.

[26]Lu, G., and Lele, S. K., "On the Density Ratio Effect on the Growth Rate of a Compressible Mixing Layer," *Physics of Fluids Brief Communication*, Vol. 6, No. 2, 1994, pp. 1073–1075.

[27]Dimotakis, P. E., "Turbulent Free Shear Layer Mixing and Combustion," *High-Speed Flight Propulsion Systems*, edited by S. N. B. Murthy and E. T. Curran, Vol. 137, Progress in Astronautics and Aeronautics, AIAA, Washington, DC, 1991, pp. 265–340.

[28]Fedioun, I., Lardjane, N., and Gökalp, I., "Revisiting Numerical Errors in Direct and Large Eddy Simulations of Turbulence: Physical and Spectral Spaces Analysis," *Journal of Computational Physics*, Vol. 174, No. 2, 2001, pp. 816–851.

[29]Lele, S. K., "Compact Finite Difference Schemes with Spectral-Like Resolution," *Journal of Computational Physics*, Vol. 103, No. 1, 1992, pp. 16–42.

[30]Jameson, A., Schmidt, H., and Turkel, E., "Numerical Solution of the Euler Equations by Finite Volume Methods Using Runge–Kutta Time Stepping Schemes," AIAA Paper 81-1259, 1981.

[31]Baum, M., Poinsot, T. J., and Thévenin, D., "Accurate Boundary Conditions for Multicomponent Reactive Flows," *Journal of Computational Physics*, Vol. 116, No. 2, 1994, pp. 247–261.

S. Aggarwal
Associate Editor